Neutron diffraction and atomistic simulation studies of Mg doped Apatite-type Oxide Ion Conductors

E. Kendrick[1], J.E.H. Sansom[1], J.R. Tolchard[2], M.S. Islam[3], P.R. Slater[1]

[1] Chemistry, UniS Materials Institute University of Surrey, Guildford, Surrey. GU2 7XH. UK

[2] Department. of Materials Technology, Norwegian University of Science and Technology, Sem Sælands vei 14, N-7491 Trondheim, Norway

[3] Department of Chemistry, University of Bath, Bath, BA2 7AY. UK

Correspondence to

Dr. P.R. Slater

Chemistry, University of Surrey, Guildford, Surrey. GU2 7XH. UK

Tel. +44 1483 686847

Fax +44 1483 686851

e-mail: p.slater@surrey.ac.uk

Abstract

In this paper, detailed studies of the effect of Mg doping in the apatite-type oxide ion conductor $La_{9.33}Si_6O_{26}$ are reported. Mg is confirmed as an ambi-site dopant, capable of substituting for both La and Si, depending on the starting composition. A large enhancement in the conductivity is observed for Si site substitution, with a reduction for substitution on the La site. Neutron powder diffraction studies show that in agreement with cation size expectations, an enlargement of the unit cell is observed on Mg substitution for Si, with a corresponding increase in the size of the tetrahedral sites. For Mg substitution on the La site, a contraction of the unit cell is observed, and the neutron diffraction results indicate that there is preferential occupancy of Mg on the La2 (1/3, 2/3, ≈0.5) site. Atomistic simulation studies show significant local structural changes affecting the oxide ion channels in both cases. Mg doping on the Si site leads to a local expansion of the channels, while doping on the La site results in a large displacement of the silicate O4 site, such that it encroaches the oxide ion channels. The observed differences in conductivities are discussed with respect to these observations.

Keywords: Oxide ion conduction, neutron diffraction, apatite, atomistic simulation, solid oxide fuel cell

Introduction

The identification and optimisation of oxide ion conductivity in solids has achieved considerable worldwide interest due to the technological applications of oxide ion conducting materials, e.g. as electrolytes for Solid Oxide Fuel Cells, O_2 separation membranes. Traditionally work has focused on materials with the fluorite (e.g. doped ZrO_2, CeO_2) or perovskite (e.g. doped $LaGaO_3$) structures [1]. Such materials are typically doped with aliovalent cations with the aim of introducing oxygen vacancies, and oxide ion conduction can then proceed via these vacant sites. The detailed research on fluorite and perovskite systems has essentially reached the state of the art that can be achieved in such structures. Therefore the search for new electrolytes has now begun to target alternative structures, and in this respect apatite-type materials have been attracting significant interest.

Research interest in this area has grown following the initial reports by Nakayama *et al.* of high oxide conductivities (>10^{-3}Scm^{-1} at 500°C) in rare earth silicates, $Ln_{10-x}Si_6O_{26+y}$, with the apatite structure [2-18]. The structure of these materials is shown in figure 1. It consists of isolated SiO_4 units with the rare earth cations located in 9 coordinate and 7 coordinate channel sites. The remaining oxide ions occupy one-dimensional channels running through the structure, which are considered as vital for the high oxide ion conduction in these materials.

Initial work in this area assumed that the conduction was mediated by oxide ion vacancies as for the fluorite, and perovskite systems. However, the weight of experimental and theoretical evidence indicates that these apatite-type materials conduct via an interstitial mechanism [19-23]. The presence of oxygen interstitials has been linked to the high observed conductivity in both oxygen excess samples, e.g.

$La_9BaSi_6O_{26.5}$, and compositions showing vacancies on the La sublattice, e.g. $La_{9.33}Si_6O_{26}$. In contrast samples which are fully stoichiometric, e.g. $La_8Ba_2Si_6O_{26}$, show poor conductivity due to a lack of interstitial oxygen site occupancy [9, 16-18]. Computer modelling and neutron powder diffraction studies have contributed significantly to the further understanding of these materials. The modelling studies identified a new energetically favourable interstitial oxide ion position at the periphery of the oxide ion channels, in the vicinity of the SiO_4 groups [19,20]. Experimental studies have provided confirmation of this position, with Leon-Reina *et al*. showing occupation of a similar site in neutron diffraction studies of the $La_{9.33+x}(Si/Ge)_6O_{26+3x/2}$ systems, and Kharton *et al.* reporting penta-coordinated Fe^{3+} in Mössbauer studies of $La_{10}Si_5FeO_{26.5}$ [21-24]. Moreover, the modelling results further suggested a complex sinusoidal conduction pathway down the channels. This pathway involves migration across the face of a silicate tetrahedral unit, coupled with considerable local relaxation of the silicate substructure (figure 2). Experimental observations of relevance to this proposed importance of the silicate substructure include the differing effects of rare earth vs Si site doping outlined below, and recent solid state ^{29}Si NMR studies, which have shown a correlation between the silicon environment and the observed conductivity [25].

In terms of doping studies, a wide range of dopants have been reported [17, 23-39],

Rare earth site: Mg, Ca, Sr, Ba, Bi, Mn, Co, Ni, Cu

Si site: Ge, Ti, P, B, Al, Ga, Mn, Co, Fe, Mg, Zn, Ni, Cu

Initial studies showed that doping with lower valent ions, e.g. B^{3+}, Al^{3+}, Ga^{3+}, on the Si site, while maintaining oxygen stoichiometry, i.e. $La_{9.33+x/3}Si_{6-x}M_xO_{26}$ (M=B, Al, Ga), leads to an enhancement in the conductivity. In contrast similar doping with lower valent ions on the La site, i.e. $La_{9.33-x/3}M_{2x/3}Si_6O_{26}$ (M=Mg, Ca, Sr, Ba)

produces no such enhancement but rather tends to lower the conductivity [31]. Aside from noting the importance of the Si site in the conduction process, the origin of this different behaviour has still not been fully explained, and so requires further study. Most recently, it has been reported that Mg, Zn doping on the Si site, i.e. $La_{9.33+2x/3}Si_{6-x}M_xO_{26}$ (M=Mg, Zn) also produces a similar large enhancement in conductivity [34, 35, 38]. Transport measurements have indicated that the conductivity is indeed due to oxide ions [34]. Mg doping is particularly interesting as this dopant can also be substituted onto the La site, i.e. $La_{9.33-x/3}Mg_{2x/3}Si_6O_{26}$, in this case leading to a reduction in conductivity. Thus Mg is an ambi-site dopant in $La_{9.33}Si_6O_{26}$, substituting on either site depending on the starting composition. It therefore provides an ideal probe for the systematic investigation of the differing effects of La versus Si site substitution. With this in mind we report here a neutron powder diffraction structural study for 4 Mg doped samples, all having the same nominal oxygen content (O_{26}), to include 2 samples doped only on the Si site, $La_{9.5}Si_{5.75}Mg_{0.25}O_{26}$, $La_{9.67}Si_{5.5}Mg_{0.5}O_{26}$, one sample doped only on the La site, $La_9Mg_{0.5}Si_6O_{26}$, and one sample doped on both the La and Si site, $La_{9.33}Mg_{0.5}Si_{5.5}Mg_{0.5}O_{26}$. The neutron diffraction work is supported by atomistic simulation studies of the local perturbations caused by a Mg dopant on the La and Si sites, and the results are correlated with conductivity measurements.

Experimental

Four Mg doped samples were synthesised, $La_{9.5}Si_{5.75}Mg_{0.25}O_{26}$, $La_{9.67}Si_{5.5}Mg_{0.5}O_{26}$, $La_9Mg_{0.5}Si_6O_{26}$, $La_{9.33}Mg_{0.5}Si_{5.5}Mg_{0.5}O_{26}$. The samples were prepared from the dried starting materials La_2O_3, SiO_2, MgO. Stoichiometric mixtures were intimately ground

and heated for 16 hours at 1350ºC with a second firing at 1400-1500ºC for a further 16 hours. Between firings the samples were reground to ensure homogeneous reaction, with phase purity being examined using a Seifert 3003TT powder X-ray diffractometer.

Conductivity measurements were performed using AC impedance spectroscopy (Solartron 1260 Impedance Analyser). Dense samples for measurement were prepared by pressing into 13mm diameter pellets and firing for 2 hours at 1550-1650ºC. Pt electrodes were then affixed to the pellets using Pt paste and the pellet fired again, at 850ºC for 30 mins, to give good electrical contact between sample and electrode.

Time of flight neutron diffraction data were recorded on diffractometer HRPD at the ISIS facility, Rutherford Appleton Laboratory. All structural refinements employed the GSAS suite of Rietveld refinement software [40].

The computational studies of the local distortions introduced by a Mg dopant on the La and Si sites were performed using well established atomistic techniques, as embodied in the GULP code [41]. These methodologies are extensively documented elsewhere [42], so only a brief summary is given here. The calculations are based on the Born model in which interactions between ions are evaluated in terms of long range Coulombic terms and short-range interactions which take account of Pauli repulsion and Van der Waals effects. To model these short-range interactions, the Buckingham potential was used:

$$V_{ij}(r_{ij}) = A\exp(-r_{ij}/\rho) - C/r_{ij}^{6} \qquad (1)$$

where r is the interatomic separation and A, ρ and C are empirically derived parameters. A well established three-body term for the angle-dependant [SiO_4]

tetrahedral unit was used [19,20]. Because charged defects will polarise other ions in the lattice, it is important to include a good description of ionic polarisability in the model. The shell model was used in this work, which describes each ion in terms of a separate core connected to a mass-less shell via a harmonic spring.

An important feature of these simulations is the treatment of lattice relaxation around the dopant Mg^{2+} ion. The Mott-Littleton approach was employed, in which the crystal lattice is partitioned into two regions: the immediate environment surrounding the defect is relaxed explicitly, whilst the remainder of the crystal, where the defect forces are relatively weak, is treated by more approximate quasi-continuum methods. In this way the local relaxation is effectively modelled and the crystal is not considered simply as a rigid lattice.

Interatomic potentials were transferred directly from our previous study of $La_{9.33}Si_6O_{26}$, which accurately reproduce the observed complex structure [19,20]. For this work, calculations were based upon a 1x1x3 supercell (124 atoms) of the $La_{9.33}Si_6O_{26}$ crystallographic unit cell, with periodic boundary conditions applied to generate the full crystal. The La vacancies were placed on the La1/La2 sites in accordance with previous experimental and simulation work, and the lattice was then allowed to relax to find the lowest energy configuration. This structural model was then used for the local structure analysis on incorporation of Mg^{2+} dopant ions onto the Si and La sites.

Results

X-ray powder diffraction showed that the four samples, $La_{9.5}Si_{5.75}Mg_{0.25}O_{26}$, $La_{9.67}Si_{5.5}Mg_{0.5}O_{26}$, $La_9Mg_{0.5}Si_6O_{26}$, $La_{9.33}Mg_{0.5}Si_{5.5}Mg_{0.5}O_{26}$, were successfully prepared confirming that Mg is an ambi-site dopant, which can be substituted onto both the La and the Si site. The bulk conductivity data (table 1) shows that doping Mg onto the Si site results in an enhancement in conductivity of an order of magnitude while doping onto the La site reduces the conductivity by a similar amount, a result which accords well with previous reports [34,35,38]. The sample, $La_{9.33}Mg_{0.5}Si_{5.5}Mg_{0.5}O_{26}$, doped on both sites displays a conductivity similar to undoped $La_{9.33}Si_6O_{26}$ as the two effects counterbalance each other. .

Structure determination

Initial Rietveld analysis of the diffraction data focussed on the determination of the appropriate symmetry for the Mg doped systems. In accordance with previous studies on apatite type materials, two space groups were examined: $P6_3/m$, and $P6_3$, with the assignment being based on the residual R-factors. For all four samples an improved fit was obtained by lowering the symmetry to $P6_3$. There was no evidence for any anisotropic peak broadening observed previously for Co doping on the Si site [32].

The Mg occupancies of the La, Si site were fixed at the value expected from the starting composition. In accordance with previous experimental observations, and predictions from modelling, the 6c La3 site was found to be fully occupied by La, with La non-stoichiometry preferring the [1/3,2/3,z] La1/La2 positions. The occupancies of these two sites were refined with the constraint that the final stoichiometry equalled the starting composition of the material. For the samples with Mg on the La site, $La_9Mg_{0.5}Si_6O_{26}$, $La_{9.33}Mg_{0.5}Si_{5.5}Mg_{0.5}O_{26}$, the presence of both

cation vacancies and dopant complicates the location of the dopant. Therefore, in the initial stages of the refinement, the Mg was distributed statistically over the La1/La2 sites. An inspection of the bond distances showed a significant difference in the La2-O distances compared to samples without Mg doping on the La site. The bond length changes were consistent with modelling predictions for Mg substituting on this site (see later) and therefore the results suggested that Mg preferentially occupies the La2 site in $La_9Mg_{0.5}Si_6O_{26}$, $La_{9.33}Mg_{0.5}Si_{5.5}Mg_{0.5}O_{26}$. In the final refinement of these two samples, therefore, the Mg was assumed to all be located on the La2 site. The number of cation vacancies on the La1/La2 sites was then refined.

In terms of the oxygen positions, the occupancy of the channel oxygen (O5) site was initially varied. In all cases, the refined site occupancy dropped below 1.0 with a value lieing between 0.84-0.90. Along with this reduced site occupancy, the anisotropic thermal displacement parameter U_{33} for O5 in all samples were very high. This suggested that there were significant displacements of the oxygens in the O5 site into interstitial positions. Therefore a number of refinements were performed to try to find the location of the remaining oxygens. Difference fourier maps suggested the presence of small levels of unfitted scattering along z close to the centre of the channels, as well as at the periphery, close to the silicate groups, in positions similar to those reported by previous modelling and neutron diffraction studies. Attempts to refine occupancy in these positions were, however, unsuccessful, which may be related to the resultant small occupancies of these sites. Therefore in the final refinements, no interstitial sites were included and the occupancies of the O5 site were fixed at 1.0 in order to achieve electroneutrality.

Final refined structural data are given in table 2, with selected bond distances in table 3. The neutron diffraction profiles are shown in figures 3-6.

To supplement the neutron diffraction studies, the local bond length changes accompanying the Mg doping were determined from atomistic simulations. These local bond length changes are shown in table 4.

Discussion

The calculated cell parameter data (table 2) were all in agreement with those expected from the dopant size. For example, doping Mg onto the La site ($La_9Mg_{0.5}Si_6O_{26}$) results in a decrease in cell size compared to $La_{9.33}Si_6O_{26}$ due to the smaller size of Mg^{2+} compared to La^{3+}. Similarly substitution on the Si site ($La_{9.5}Si_{5.75}Mg_{0.25}O_{26}$, $La_{9.67}Si_{5.5}Mg_{0.5}O_{26}$) results in a significant increase in the cell size as Mg^{2+} is larger than Si^{4+}. The sample doped with Mg on both sites ($La_{9.33}Mg_{0.5}Si_{5.5}Mg_{0.5}O_{26}$) has cell parameters in between those of the single site doped samples $La_9Mg_{0.5}Si_6O_{26}$ and $La_{9.67}Si_{5.5}Mg_{0.5}O_{26}$.

All four Mg doped samples were refined with space group $P6_3$. The lowering of symmetry from $P6_3/m$ to $P6_3$ leads to a splitting of some of the crystallographic sites, and there was evidence for ordering of La vacancies/Mg in the split La sites. In particular Mg was shown to occupy the La2 (1/3, 2/3, ≈0.5) position in preference to La1 (1/3, 2/3, ≈0.0). In addition the former site generally contained more cation vacancies than the latter. For example in the case of the sample $La_{9.33}Mg_{0.5}Si_{5.5}Mg_{0.5}O_{26}$, the occupancy of the La1 site refined to 1.0 indicating no vacancies on this site, with all the vacancies correspondingly on the La2 site.

A comparison of the bond distances for the Mg doped samples shows that on doping on the Si site an expansion of the tetrahedra is observed (table 3) in agreement with

the larger size of Mg^{2+} compared to Si^{4+}. Atomistic simulation studies indicate that Mg doping results in a large local distortion, with the predicted Mg-O bond distances ranging between 1.84 and 1.96 Å (table 4). This corresponds to an average 17 % expansion in the tetrahedra.

In the case of Mg doping on the La site, the observed data show that the La2-O bond distances change significantly, indicating that Mg substitutes preferentially on this site. From the data it can be seen that six of the bonds (La2-O1, O2) shorten while there is a lengthening of the remaining three (La2-O4). This has the effect of creating further distortion in the coordination of this site, such that the original distorted nine coordination environment approaches six coordination, with the remaining three bonds being very long. The neutron diffraction results are in complete agreement with atomistic simulation predictions, which show that the introduction of the small Mg^{2+} cation on the La site causes a large change in the bond distances (table 4) resulting in an effective 6 coordination for the Mg.

Apart from the bond distance and cell parameter changes due to the dopant Mg, reported above, there are no other significant structural differences between the four samples. In all four samples, very high thermal displacement parameters are observed for the O5 channel oxygen site consistent with previous structural studies of apatite-type rare earth silicates/germinates [9, 21-23]. These thermal displacement parameters are highly anisotropic, with U_{33} (corresponding to the direction of the oxygen channels) being particularly large. As noted in the structural determination section, the freely refined occupancy of this site drops below 1.0. This coupled with the high thermal displacement parameters indicates significant displacement of oxygens into interstitial sites. Difference fourier maps were investigated to locate the exact positions of the interstitial sites, and indicated small regions of unfitted scattering

along the channels near to the channel centre, along with regions at the periphery of the channels in positions similar to the favourable interstitial site predicted by our modelling studies of $La_{9.33}Si_6O_{26}$ [19,20], and subsequently reported in neutron diffraction studies of $La_{9.33+x}(Si/Ge)_6O_{26+3x/2}$ by Leon-Reina *et al*. [21-23]. However, attempts to refine occupancy in these sites were unsuccessful, which may be due to the displaced oxygens being distributed over not just one, but a range of interstitial sites, leading to low occupancies for each site.

In addition to the high thermal displacement parameters for the O5 site, the values for the silicate tetrahedra oxygens (O1-O4) are also high, which are also consistent with previous structural studies [9, 21-23]. It should be noted that the presence of Mg on the Si site would be expected to produce an increase in these parameters due to the significantly longer Mg-O bond distances compared to Si-O, but nevertheless the dopant levels are relatively low and so the high thermal displacement parameters are unlikely to simply be correlated with the effect of the dopant. Moreover, high values are also observed for the sample without Si site doping. In terms of the other sites, the thermal parameters for the La1 site are also relatively high, which may be related to the local distortions caused by neighbouring La vacancies and/or Mg in the adjacent La2 site.

Overall the results suggest significant structural distortions in these Mg doped apatite-type lanthanum silicates. However from the structural parameters derived from neutron diffraction, there is no clear indication why the samples doped with Mg on the La site have significantly lower conductivities than the samples doped on the Si site. This deficiency can be correlated with the fact that neutron diffraction only gives an average structure, and since the dopant levels are relatively low, the structural changes observed are masked within this average structure. In order to determine the

origin of the conductivity differences, we therefore need to analyse the *local* structural changes, and in this respect the atomistic simulation studies provide detailed results. These atomistic simulation studies show the structural changes occurring in the vicinity of a dopant Mg^{2+} cation, whether it is on the La or the Si site.

The modelled local environments for the undoped, Mg on Si site, and Mg on La2 site systems are shown in figures 7-9. As outlined above, doping with Mg on the Si site leads to an expansion of the tetrahedra. In addition to affecting the tetrahedral site, such large changes also have a large affect on the surrounding sites (table 4, Figure 8). In particular, it is seen that the La1/La2-O distances to the oxygens of the MgO_4 tetrahedra all shorten to a similar length (≈2.4 Å). In addition there is a change in the tilting of the tetrahedra (MgO_4) with respect to the O5 channels as well as an increase in the average distance between the O5 site and O1,O3,O4 sites (average distance = 3.82 Å (Mg on Si site) versus 3.56 Å (undoped)). The latter indicates that Mg doping for Si leads to an expansion of the oxide ion channels, while the former results in more of the O1-O3-O4 face showing to the channel. Since the predicted interstitial oxide ion sites are at the periphery of the channels near the silicate tetrahedra, and their conduction pathway involves migration across the face of a silicate tetrahedral unit, then both the above local structural changes might account for the observed increase in conductivity by enhancing the favourability of the interstitial oxide ion defects as well as lowering their migration energy. In addition, the ability of Mg to expand its coordination sphere might also enhance the conductivity for samples doped with Mg on the Si site.

In contrast to the beneficial effects of Mg doping on the Si site, the incorporation of a Mg^{2+} dopant cation on the La site leads to a significant reduction in conductivity. The simulation data shows that the incorporation of Mg on the La2 site results in a

large change in the bond distances of this site (table 4, figure 9). In particular six of the bonds (La2-O1,O2) shorten, while the remaining three (La2-O4) lengthen considerably. The overall effect is that the coordination of the site changes from a distorted 9 coordinate environment to an effective 6 coordinate environment for Mg. The effect of the large (0.45 Å) expansion in the La2-O4 distance is to cause the O4 site to encroach the oxide ion channels, as can be seen from the significant reduction in the O5-O4 distance (from 3.255 to 2.954 Å). In addition this reduction in O5-O4 distance results in a significant change in the tilting of the adjacent SiO_4 tetrahedra, such that the oxide ion channels see less of the O1-O3-O4 face, as evidenced by the large differences in the O1-O5, O3-O5, O4-O5 distances, which vary between 2.95 and 4.13 Å (cf the much smaller variation for Mg doping on the Si site, 3.72-3.86 Å). Both these structural changes might be expected to adversely affect the generation of interstitial oxide ion defects as well as their migration, accounting for the reduction in conductivity.

Conclusions

Mg has been successfully doped into the apatite-type lanthanum silicate, $La_{9.33}Si_6O_{26}$, substituting onto either the La or Si site depending on the starting stoichiometry. In agreement with cation size expectations, an enlargement of the unit cell is observed on Mg substitution for Si, with a contraction of the unit cell for Mg substitution on the La site. For the latter, the neutron diffraction results indicate that there is ordering of Mg on the La2 (1/3, 2/3, ≈0.5) site, with corresponding significant changes in the bond lengths for this site, consistent with predictions from atomistic simulation studies that the coordination effectively reduces from a distorted nine coordination to

six coordination. These atomistic simulation studies show that both doping strategies influence the oxide ion channels, with Mg doping on the Si site leading to a local expansion of the channels, while doping on the La site results in a large displacement of the silicate O4 site, such that it encroaches the oxide ion channels. The observed local structural changes are therefore consistent with Mg doping on the Si site enhancing the conductivity, while La site doping reduces it.

Acknowledgements

The authors would like to thank EPSRC for funding this work. We would also like to express thanks to ISIS for neutron diffraction beam time and to Kevin Knight for his help in the neutron data collection.

References

1. J.B. Goodenough; *Annu. Rev. Mater. Res*. 2003, **33,** 91.

2. S. Nakayama, H. Aono, Y. Sadaoka, *Chem. Lett.* 1995, 431.

3. S. Nakayama, M. Sakamoto, *J. Eur. Ceram. Soc*. 1998, **18,** 1413.

4. S. Nakayama, M. Sakamoto, M. Higuchi, K. Kodaira, M. Sato, S. Kakita, T. Suzuki, K. Itoh, *J. Eur. Ceram. Soc*. 1999, **19,** 507.

5. M. Higuchi, H. Katase, K. Kodaira, S. Nakayama; *J. Cryst. Growth* 2000, **218,** 218.

6. S. Nakayama, M. Sakamoto, M. Higuchi, K. Kodaira, *J. Mater. Sci. Lett*. 2000, **19**, 91.

7. S. Nakayama, M. Niguchi; *J. Mater. Sci. Lett.* 2001, **20**, 913.

8. S. Tao, J.T.S. Irvine, *Mater. Res. Bull.* 2001, **36**, 1245.

9. J.E.H. Sansom, D. Richings, P.R. Slater, *Solid State Ionics* 2001, **139**, 205.

10. H. Arikawa, H. Nishiguchi, T. Ishihara, Y. Takita, *Solid State Ionics* 2000, **136-137**, 31.

11. J.E.H. Sansom, L. Hildebrandt, P.R. Slater, *Ionics* 2002, **8,** 155.

12. S. Nakayama and M. Sakamoto; *J. Mater. Sci. Lett*. 2001, **20**, 1627.

13. P. Berastegui, S. Hull, F.J. Garcia Garcia and J. Grins; *J. Solid State Chem*. 2002, **168**, 294.

14. L. Leon-Reina, M.E. Martin-Sedeno, E.R. Losilla, A. Caberza, M. Martinez-Lara, S. Bruque, F.M.B. Marques, D.V. Sheptvakov, M.A.G. Aranda; *Chem. Mater.* 2003, **15**, 2099.

15. E.J. Abram, C.A. Kirk, D.C. Sinclair, A.R. West; *Solid State Ionics* 2005, **176**, 1941.

16. Y. Masubuchi, M. Higuchi, S. Kikkawa, K. Kodaira, S. Nakayama; *Solid State Ionics* 2004, **175**, 357.

17. P.R. Slater, J.E.H. Sansom; *Solid State Phenomena* 2003, **90-91**, 195.

18. Y. Masubuchi, M. Higuchi, H. Katase, T. Takeda, S. Kikkawa, K. Kodaira, S. Nakayama; *Solid State Ionics* 2004, **166**, 213.

19. M.S. Islam, J.R. Tolchard, P.R. Slater; *Chem. Commun.* 2003, 1486.

20. J.R. Tolchard, M.S. Islam, P.R. Slater; *J. Mater. Chem*. 2003, **13**, 1956.

21. L. Leon-Reina, E.R. Losilla, M. Martinez-Lara, S. Bruque, M.A.G. Aranda; *J. Mater. Chem*. 2004, **14,** 1142.

22. L. Leon-Reina, E.R. Losilla, M. Martinez-Lara, M.C. Martin-Sedeno, S. Bruque, P.Nunez, D.V. Sheptyakov, M.A.G. Aranda; *Chem. Mater*. 2005, **17**, 596.

23. L. Leon-Reina, E.R. Losilla, M. Martinez-Lara, S. Bruque, A. Llobet, D.V. Sheptyakov, M.A.G. Aranda; *J. Mater. Chem*. 2005, **15**, 2489.

24. V.V. Kharton, A.L. Shaula, M.V. Patrakeev, J.C. Waerenborgh, D.P. Rojas, N.P. Vyshatko, E.V. Tsipis, A.A. Yaremchenko, F.M.B. Marques; *J. Electrochem. Soc.* 2004, **151,** A1236.

25. J.E.H. Sansom, J.R. Tolchard, D. Apperley, M.S. Islam, P.R. Slater; *J. Mater. Chem.* 2006, DOI 10.1039/b600122j.

26. E.J. Abram, D.C. Sinclair, A.R. West, *J. Mater. Chem*. 2001, **11**, 1978.

27. J. McFarlane, S. Barth, M. Swaffer, J.E.H. Sansom, P.R. Slater, *Ionics* 2002, **8**, 149.

28. J.R. Tolchard, J.E.H. Sansom, P.R. Slater and M.S. Islam; *Solid State Ionics* 2004, **167,** 17.

29. A.L. Shaula, V.V. Kharton, M.V. Patrakeev, J.C. Waerenborgh, D.P. Rojas, N.P. Vyshatko, E.V. Tsipis, A.A. Yaremchenko, F.M.B. Marques; *Mater. Res. Bull.* 2004, **39**, 763.

30. A.A. Yaremchenko, A.L. Shaula, V.V. Kharton, J.C. Waerenborgh, D.P. Rojas, M.V. Patrakeev, F.M.B. Marques; *Solid State Ionics* 2004, **171,** 51.

31. A. Najib, J.E.H. Sansom, J.R. Tolchard, M.S. Islam, P.R. Slater; *Dalton Trans*. 2004, **19**, 3106.

32. J.R. Tolchard, J.E.H. Sansom, M.S. Islam, P.R. Slater; *Dalton Trans* 2005, **20**, 1273.

33. J. R. Tolchard, P. R. Slater and M. S. Islam; manuscript in preparation.

34. H. Yoshioka, S. Tanase; *Solid State Ionics* 2005, **176**, 2395.

35. H. Yoshioka; *Chem. Lett*. 2004, **33,** 392.

36. J.E.H. Sansom and P.R. Slater; *Proc. 5th Euro SOFC forum* 2002, **2**, 627.

37. J.E.H. Sansom, P.A. Sermon, P.R. Slater; *Solid State Ionics* 2005, **176**, 1765.

38. J.E.H. Sansom, E. Kendrick, J.R. Tolchard, M.S. Islam, P.R. Slater; *J. Solid State Electrochem* (in press).

39. J.E.H. Sansom, P.A. Sermon, P.R. Slater; unpublished work.

40. A.C. Larson, R.B. Von Dreele. *Los Alamos National Laboratory, Report*. No LA-UR-86-748, 1987.

41. J.D. Gale, *J. Chem. Soc. Faraday Trans*. 1997, **93**, 629.

42. C.R.A. Catlow, *Computer Modelling in Inorganic Crystallography*, Academic Press, San Diego, 1997.

Table 1. Conductivity data for Mg doped $La_{9.33}Si_6O_{26}$ samples.

Sample	σ (Scm^{-1}) at 500°C	E_a (eV)
$La_{9.33}Si_6O_{26}$	1.1×10^{-4}	0.74
$La_{9.5}Si_{5.75}Mg_{0.25}O_{26}$	1.8×10^{-3}	0.68
$La_{9.67}Si_{5.5}Mg_{0.5}O_{26}$	3.0×10^{-3}	0.67
$La_9Mg_{0.5}Si_6O_{26}$	2.1×10^{-5}	0.98
$La_{9.33}Mg_{0.5}Si_{5.5}Mg_{0.5}O_{26}$	1.6×10^{-4}	0.80

Table 2a Atomic parameters for $La_{9.33}Mg_{0.5}Si_{5.5}Mg_{0.5}O_{26}$, $La_{9.5}Si_{5.75}Mg_{0.25}O_{26}$, $La_{9.67}Si_{5.5}Mg_{0.5}O_{26}$, and $La_9Mg_{0.5}Si_6O_{26}$.

	$La_{9.33}Mg_{0.5}Si_{5.5}Mg_{0.5}O_{26}$	$La_{9.5}Si_{5.75}Mg_{0.25}O_{26}$	$La_{9.67}Si_{5.5}Mg_{0.5}O_{26}$	$La_9Mg_{0.5}Si_6O_{26}$
	La/Si-0.5Mg	Si-0.25Mg	Si-0.5Mg	La-0.5Mg
a, b	9.70929(2)	9.72332(2)	9.73415(1)	9.69054(2)
c	7.16094(4)	7.19329(2)	7.21605(2)	7.13692(2)
Rwp	0.0835	0.0731	0.065	0.0857
χ^2	1.662	1.145	1.07	1.244
La1, 2b, (1/3, 2/3, z)				
SOF	1.0	0.92(3)	0.93(4)	0.94(3)
Z	-0.007(2)	-0.003(1)	-0.003(1)	-0.005(2)
La2/Mg, 2b, (1/3, 2/3, z)				
SOF	0.6667 / 0.25	0.83(3)	0.91(4)	0.56(3) / 0.25
Z	0.492(2)	0.496(1)	0.496(1)	0.494(2)
La3, 6c, (x, y, z)				
X	0.2412(1)	0.2410(1)	0.24159(9)	0.2438(1)
Y	0.0113(2)	0.0123(1)	0.0120(1)	0.0130(2)
Z	0.241(1)	0.243(1)	0.2428(9)	0.245(1)
Si /Mg, 6c, (x ,y, 0.25)				
SOF	0.9167 / 0.0833	0.9583 / 0.0417	0.9167 / 0.0833	1
X	0.3746(3)	0.3720(2)	0.3731(2)	0.3733(2)
Y	0.3995(3)	0.3994(2)	0.4011(2)	0.4014(3)
O1, 6c, (x, y, z)				
X	0.4910(2)	0.4858(2)	0.4876(2)	0.4881(3)
Y	0.3296(3)	0.3249(2)	0.32570(2)	0.3262(1)
z	0.240(2)	0.245(1)	0.246(1)	0.243(2)
O2, 6c, (x, y, z)				
x	0.4701(2)	0.4721(2)	0.4716(1)	0.4703(2)
y	0.5987(3)	0.5964(2)	0.5977(2)	0.5948(2)
z	0.243(2)	0.247(1)	0.247(1)	0.249(2)
O3, 6c, (x, y, z)				
x	0.2579(7)	0.2581(6)	0.2569(6)	0.2551(8)
y	0.3534(6)	0.3516(6)	0.3515(6)	0.3507(8)
z	0.054(1)	0.058(1)	0.058(1)	0.060(2)
O4, 6c, (x, y, z)				
x	0.2543(6)	0.2527(5)	0.2540(5)	0.2539(7)
y	0.3312(9)	0.3369(7)	0.3392(7)	0.3309(10)
z	0.414(1)	0.419(1)	0.421(1)	0.418(2)
O5, 2a, (0, 0, z)				
z	0.248(5)	0.256(4)	0.250(3)	0.249(4)

[a] All Oxygen (O1-O5) and La3 sites are fully occupied,

Table 2b Anisotropic thermal displacement paramters for $La_{9.33}Mg_{0.5}Si_{5.5}Mg_{0.5}O_{26}$, $La_{9.5}Si_{5.75}Mg_{0.25}O_2$, $La_{9.67}Si_{5.5}Mg_{0.5}O_{26}$, and $La_9Mg_{0.5}Si_6O_{26}$. ($La_{9.33+2x/3-2y/3}Mg_ySi_{6-x}Mg_xO_{26}$)

x,y	x,y=0.5	x=0.25	x=0.5	y=0.5		x,y=0.5	x=0.25	x=0.5	y=0.5
La1					O1				
U_{11}	2.7(3)	1.9(3)	1.7(3)	2.0(3)	U_{11}	2.4(1)	3.0(1)	2.62(8)	3.1(1)
U_{22}	2.7(3)	1.9(3)	1.7(3)	2.0(3)	U_{22}	5.4(2)	4.4(1)	4.50(8)	4.2(1)
U_{33}	2.9(6)	3.6(4)	2.5(4)	4.3(5)	U_{33}	4.0(2)	2.5(1)	2.07(9)	4.1(1)
U_{12}	1.4(1)	0.9(2)	0.8(2)	1.0(2)	U_{12}	2.6(1)	2.75(9)	2.48(7)	2.9(1)
U_{13}	0	0	0	0	U_{13}	0.7(4)	0.2(3)	0.2(3)	1.6(6)
U_{23}	0	0	0	0	U_{23}	-1.4(4)	-1.5(3)	-1.2(3)	-0.3(4)
La2					O2				
U_{11}	0.7(2)	1.0(3)	1.5(3)	0.6(3)	U_{11}	1.4(1)	1.48(8)	1.27(7)	1.60(9)
U_{22}	0.7(2)	1.0(3)	1.5(3)	0.6(3)	U_{22}	2.0(1)	1.75(8)	1.66(7)	1.56(9)
U_{33}	1.6(5)	1.3(4)	1.0(3)	1.0(4)	U_{33}	6.0(2)	3.6(1)	3.37(9)	6.3(2)
U_{12}	0.4(1)	0.5(2)	0.8(2)	0.3(2)	U_{12}	0.30(9)	0.31(7)	0.36(6)	0.35(8)
U_{13}	0	0	0	0	U_{13}	-0.5(4)	1.4(2)	1.0(3)	-0.2(5)
U_{23}	0	0	0	0	U_{23}	1.8(4)	-0.4(2)	-0.4(2)	-0.4(5)
La3					O3				
U_{11}	1.79(7)	1.77(6)	1.66(5)	1.65(6)	U_{11}	3.9(3)	4.1(2)	4.0(2)	3.7(3)
U_{22}	1.64(6)	1.56(5)	1.54(4)	1.52(6)	U_{22}	3.9(2)	3.4(2)	3.0(2)	5.2(3)
U_{33}	1.60(6)	1.55(5)	1.44(4)	1.49(5)	U_{33}	1.9(3)	2.0(2)	2.3(2)	2.1(3)
U_{12}	0.69(6)	0.72(5)	0.82(4)	0.82(6)	U_{12}	2.8(2)	2.8(2)	2.6(2)	2.9(3)
U_{13}	-0.3(2)	0.5(2)	0.4(2)	0.5(2)	U_{13}	-0.4(2)	-0.4(2)	-0.1(2)	-0.6(2)
U_{23}	-0.3(3)	0.1(2)	0.22(2)	0.3(3)	U_{23}	-0.9(2)	-1.2(1)	-0.6(1)	-1.0(2)
Si					O4				
U_{11}	2.0(1)	1.8(1)	1.54(8)	1.3(1)	U_{11}	0.7(2)	0.2(2)	0.7(2)	0.8(2)
U_{22}	2.3(1)	2.1(1)	1.57(8)	1.5(1)	U_{22}	12.1(5)	8.9(4)	7.6(3)	11.9(5)
U_{33}	3.2(2)	2.7(1)	1.7(1)	2.5(2)	U_{33}	2.2(3)	1.7(2)	1.4(2)	1.8(2)
U_{12}	0.9(1)	0.96(9)	0.53(7)	0.6(1)	U_{12}	2.1(3)	1.0(2)	1.3(2)	2.5(3)
U_{13}	2.0(3)	0.6(3)	0.9(2)	1.6(4)	U_{13}	0.5(2)	0.4(2)	0.3(2)	0.6(2)
U_{23}	-1.8(3)	-2.6(2)	-1.3(3)	0.4(4)	U_{23}	3.4(3)	1.9(2)	1.9(2)	3.5(3)
					O5				
					U_{11}	2.2(1)	2.09(9)	1.77(7)	1.97(10)
					U_{22}	2.2(1)	2.09(9)	1.77(7)	2.0(1)
					U_{33}	14.6(6)	15.2(6)	10.7(3)	11.3(4)
					U_{12}	1.08(6)	1.05(4)	0.89(3)	0.99(5)
					U_{13}	0	0	0	0
					U_{23}	0	0	0	0

Table 3. Bond lengths for $La_{9.33}Mg_{0.5}Si_{5.5}Mg_{0.5}O_{26,}$ $La_{9.5}Si_{5.75}Mg_{0.25}O_{2,}$ $La_{9.67}Si_{5.5}Mg_{0.5}O_{26,}$ and $La_9Mg_{0.5}Si_6O_{26}$.

	$La_{9.33}Mg_{0.5}Si_{5.5}Mg_{0.5}O_{26}$	$La_{9.5}Si_{5.75}Mg_{0.25}O_{26}$	$La_{9.67}Si_{5.5}Mg_{0.5}O_{26}$	$La_9Mg_{0.5}Si_6O_{26}$
La1_O1 x3	2.479(8)	2.498(7)	2.487(7)	2.479(10)
La1_O2 x3	2.503(9)	2.534(7)	2.534(7)	2.538(11)
La1_O3 x3	2.783(5)	2.805(5)	2.806(5)	2.801(6)
La2_O1 x3	2.447(8)	2.486(6)	2.486(6)	2.460(9)
La2_O2 x3	2.503(10)	2.534(6)	2.528(6)	2.496(11)
La2_O4 x3	3.002(8)	2.948(6)	2.931(6)	2.995(9)
La3_O1	2.818(3)	2.769(2)	2.790(2)	2.761(2)
La3_O2	2.525(2)	2.522(2)	2.513(1)	2.519(2)
La3_O3	2.635(6)	2.641(5)	2.627(5)	2.622(7)
La3_O3	2.443(7)	2.461(5)	2.469(5)	2.436(7)
La3_O4	2.570(6)	2.576(5)	2.586(5)	2.584(6)
La3_O4	2.473(7)	2.477(5)	2.479(5)	2.453(7)
La3_O5	2.290(1)	2.288(1)	2.3007(8)	2.298(1)
Si1_O1	1.584(3)	1.598(3)	1.612(2)	1.601(3)
Si1_O2	1.677(4)	1.660(3)	1.658(2)	1.622(3)
Si1_O3	1.720(9)	1.687(7)	1.701(7)	1.680(10)
Si1_O4	1.551(8)	1.577(6)	1.588(6)	1.565(9)

Table 4. Calculated local inter-atomic separations on incorporation of Mg on the La2 or Si site.

	Undoped	Mg on La2	Mg on Si
La2-O1	2.44	2.30	2.48
La2-O1	2.44	2.30	2.48
La2-O1	2.44	2.30	2.63
La2-O2	2.54	2.27	2.34
La2-O2	2.54	2.27	2.46
La2-O2	2.54	2.27	2.63
La2-O4	2.92	3.37	2.45
La2-O4	2.92	3.37	3.31
La2-O4	2.92	3.38	3.35
La1-O1	2.43	2.51	2.46
La1-O1	2.43	2.51	2.48
La1-O1	2.43	2.51	2.58
La1-O2	2.65	2.70	2.42
La1-O2	2.65	2.70	2.66
La1-O2	2.65	2.70	2.78
La1-O3	2.67	2.55	2.44
La1-O3	2.67	2.55	2.77
La1-O3	2.67	2.55	2.88
Si-O1	1.59	1.59	1.84
Si-O2	1.64	1.63	1.92
Si-O3	1.64	1.67	1.96
Si-O4	1.63	1.62	1.91
O3-O5	3.47	3.56	3.86
O4-O5	3.26	2.95	3.72
O1-O5	3.95	4.13	3.86

Figure captions

Figure 1. The apatite structure, $Ln_{10-x}(SiO_4)_6O_{2+z}$ (Dark Spheres = Ln, Tetrahedra = SiO_4, Light Spheres = O)

Figure 2. Oxygen interstitial (white spheres) migration pathway through the apatite-type system, $La_{9.33}Si_6O_{26}$ (tetrahedra = SiO_4), looking down the oxide ion channels [19].

Figure 3. Fitted neutron diffraction data for $La_{9.33}Mg_{0.5}Si_{5.5}Mg_{0.5}O_{26}$

Figure 4. Fitted neutron diffraction data for $La_{9.5}Si_{5.75}Mg_{0.25}O_{26}$

Figure 5 Fitted neutron diffraction data for $La_{9.67}Si_{5.5}Mg_{0.5}O_{26}$

Figure 6. Fitted neutron diffraction data for $La_9Mg_{0.5}Si_6O_{26}$

Figure 7. Atomic configuration of La1 and La2 polyhedra above the O5 channel with no dopant from atomistic modelling calculations.

Figure 8. Atomic configuration of La1 and La2 polyhedra above the O5 channel with Mg doping on the Si site from atomistic modelling calculations. Note the shortened distances between the La1/La2 sites and the O4, O3, O2 sites around the Mg dopant.

Figure 9. Atomic configuration of La1 and La2 polyhedra above the O5 channel with Mg on the La2 site from atomistic modelling calculations. Note the large Mg-O4 distance causing the O4 site to encroach the oxide ion channels.

Fig 1

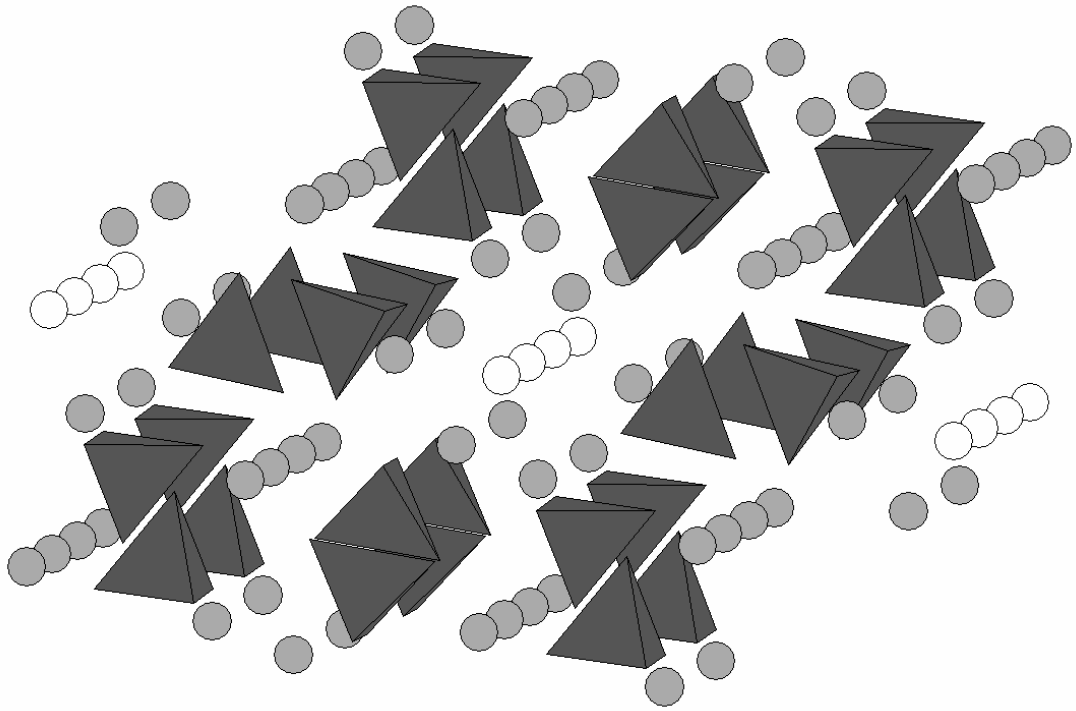

Fig 2

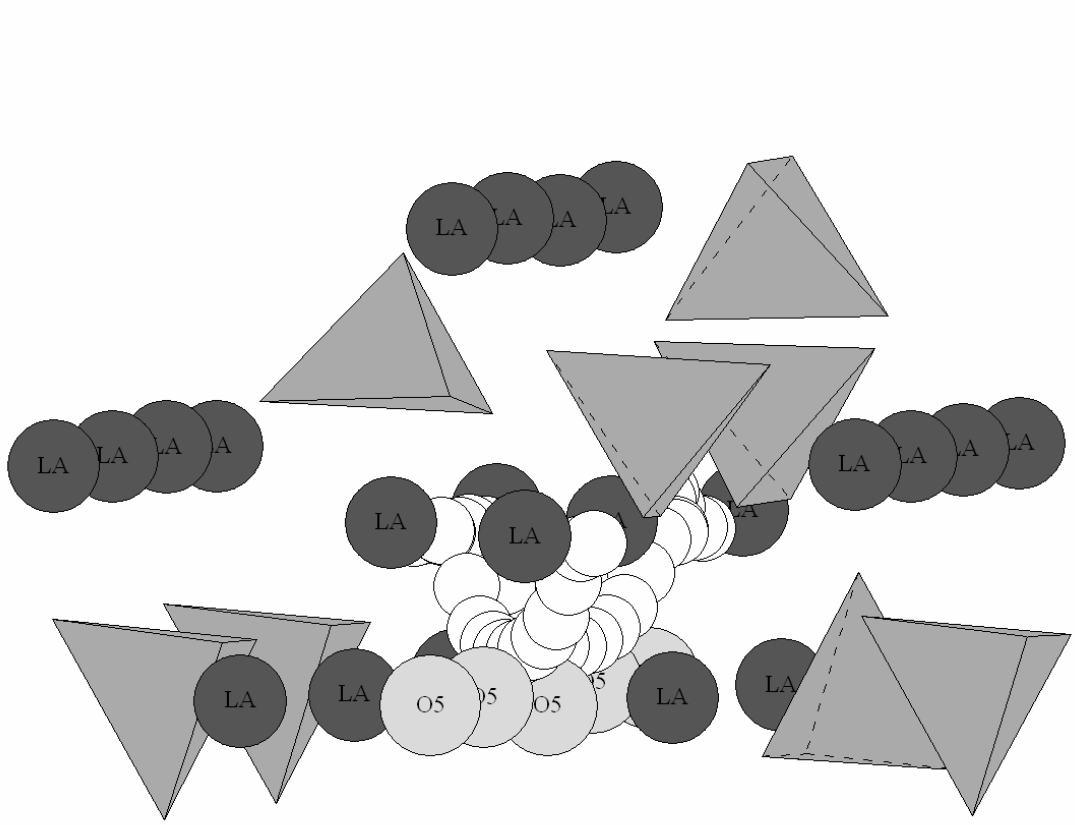

Fig 3

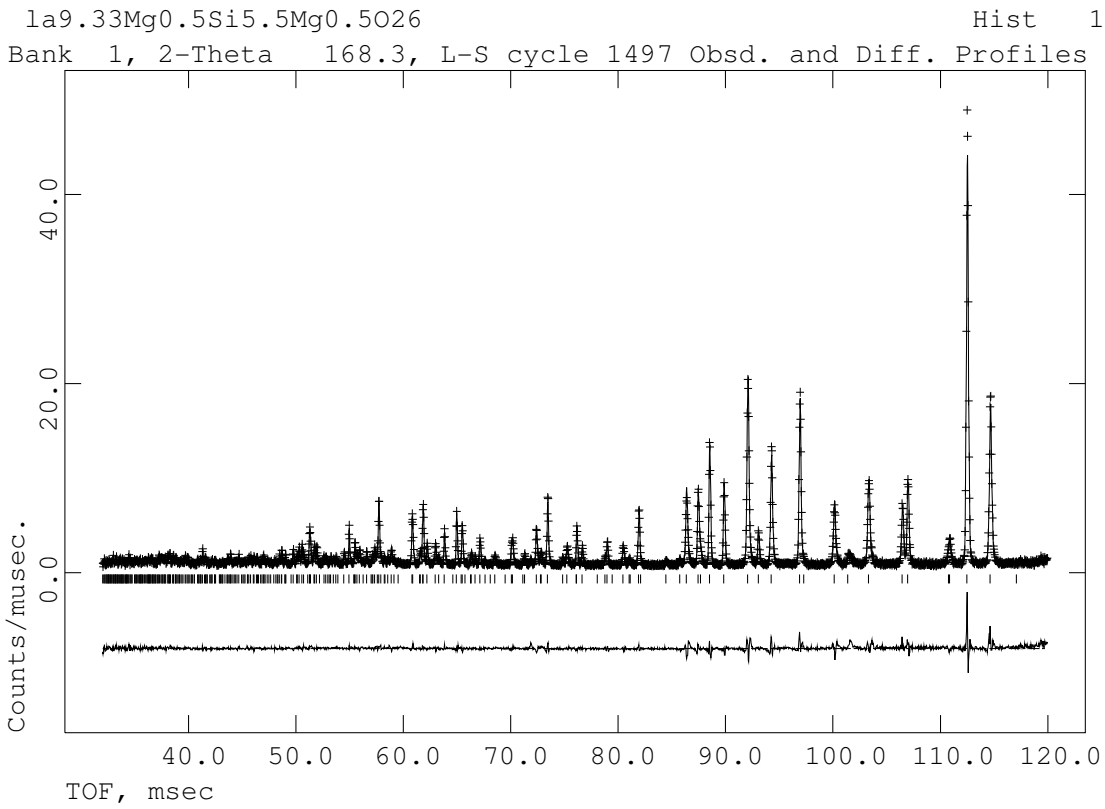
la9.33Mg0.5Si5.5Mg0.5O26 Hist 1
Bank 1, 2-Theta 168.3, L-S cycle 1497 Obsd. and Diff. Profiles
Counts/musec.
0.0
20.0
40.0
40.0 50.0 60.0 70.0 80.0 90.0 100.0 110.0 120.0
TOF, msec

Fig 4

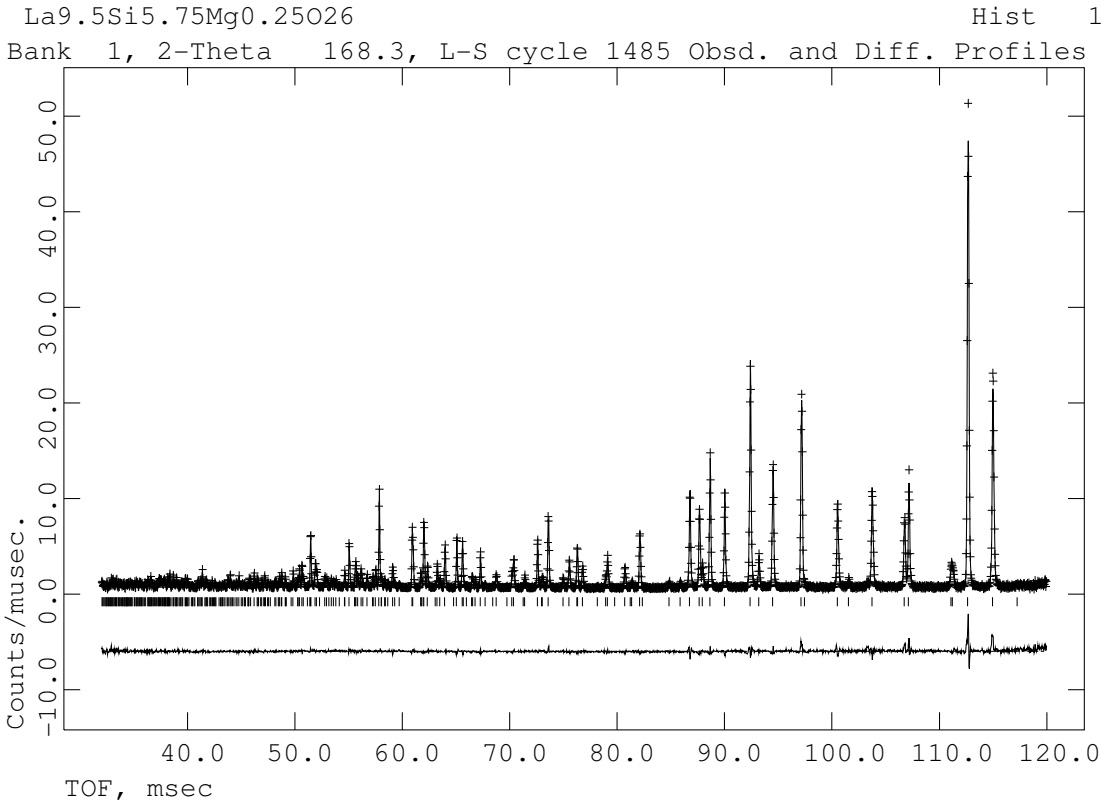
La9.5Si5.75Mg0.25O26
Hist 1
Bank 1, 2-Theta 168.3, L-S cycle 1485 Obsd. and Diff. Profiles
Counts/musec.
-10.0
0.0
10.0
20.0
30.0
40.0
50.0
40.0
50.0
60.0
70.0
80.0
90.0
100.0
110.0
120.0
TOF, msec

Fig 5

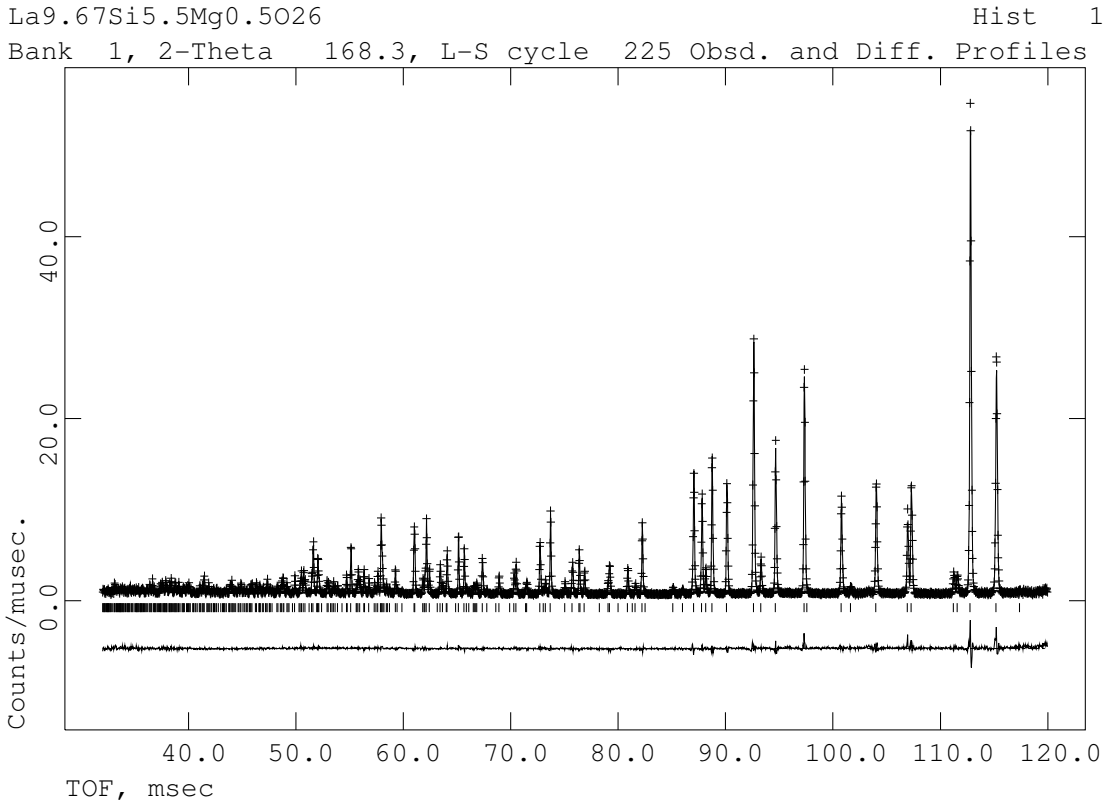
La9.67Si5.5Mg0.5O26 Hist 1
Bank 1, 2-Theta 168.3, L-S cycle 225 Obsd. and Diff. Profiles
Counts/musec.
0.0
20.0
40.0
40.0 50.0 60.0 70.0 80.0 90.0 100.0 110.0 120.0
TOF, msec

Fig 6

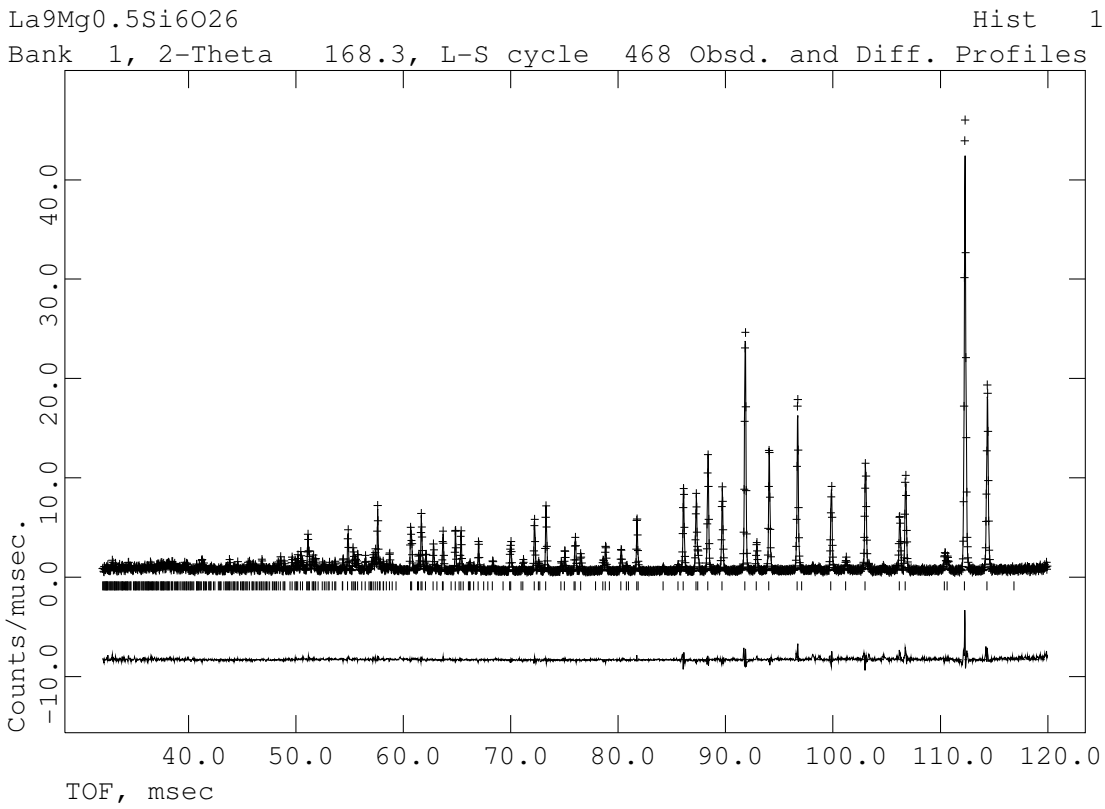
La9Mg0.5Si6O26
Hist 1
Bank 1, 2-Theta 168.3, L-S cycle 468 Obsd. and Diff. Profiles
Counts/musec.
-10.0
0.0
10.0
20.0
30.0
40.0
40.0
50.0
60.0
70.0
80.0
90.0
100.0
110.0
120.0
TOF, msec

Fig 7

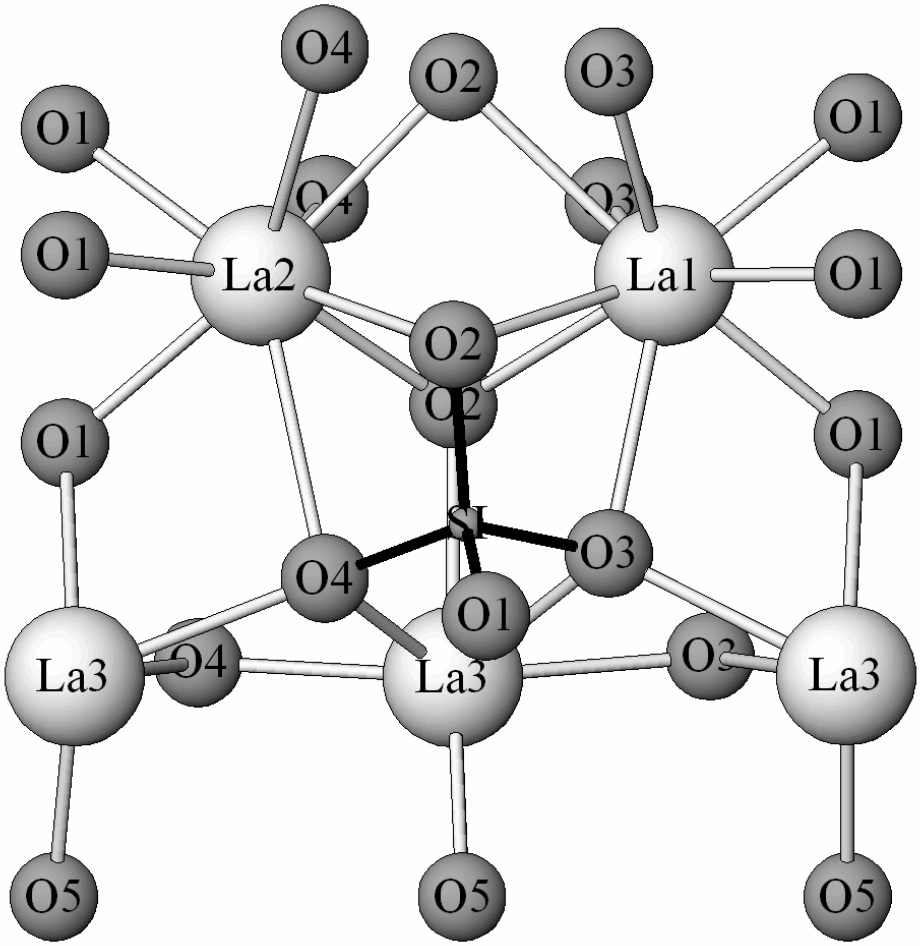
O4
O2
O3
O1
O1
O4
O3
O1
La2
La1
O1
O2
O2
O1
Si
O3
O4
O1
La3
O4
La3
O3
La3
O5
O5
O5

Fig 8.

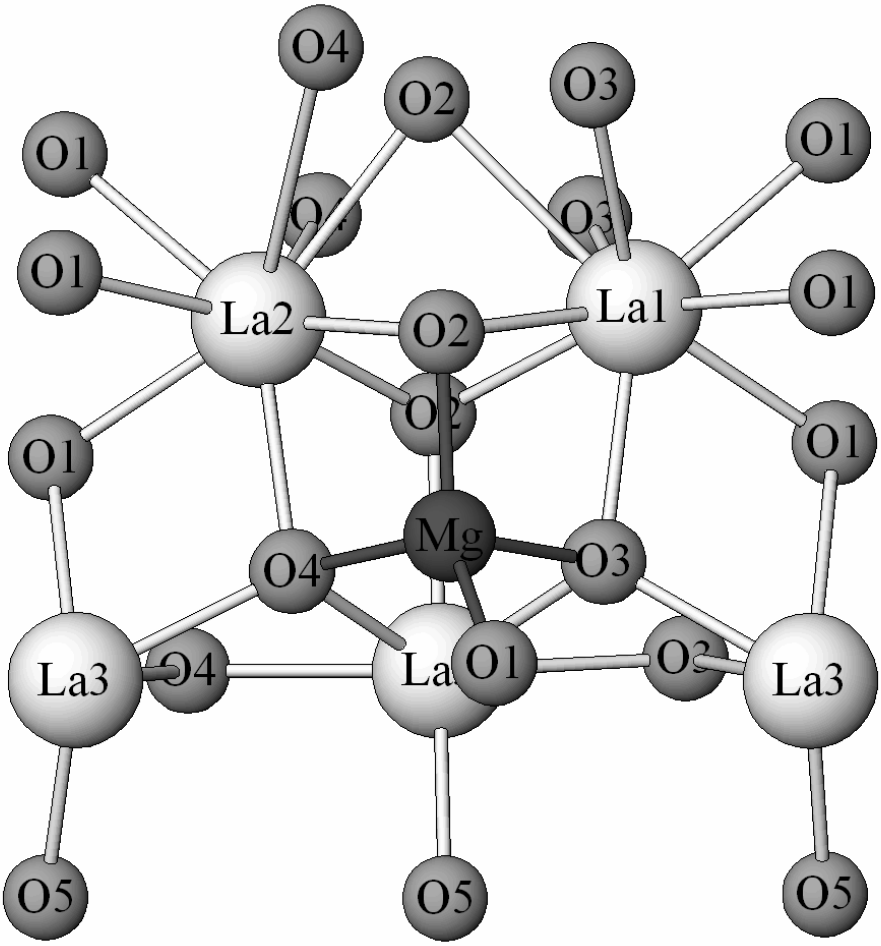
O4
O2
O3
O1
O1
O4
O3
O1
La2
O2
La1
O1
O2
O1
O1
Mg
O4
O3
La3
O4
La
O1
O2
La3
O5
O5
O5

Fig 9

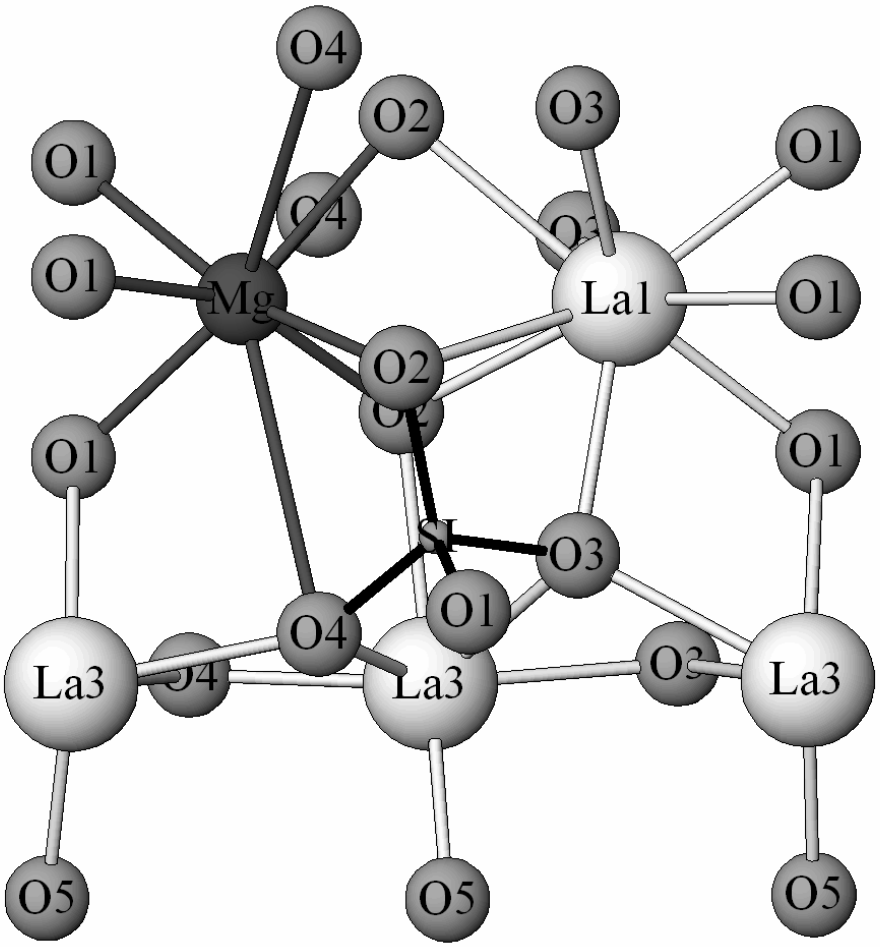
O4
O2
O3
O1
O1
O4
O3
O1
Mg
La1
O1
O2
O2
O1
O1
Si
O3
O1
O4
La3
O4
La3
O2
La3
O5
O5
O5